

# Numerical and Experimental Study of Centrifugally Driven Flow Inside a Rotating Duct

Byung-Young Min\*

United Technologies Research Center, East Hartford, Connecticut 06108

Anand Karpatne<sup>†</sup>

University of Texas at Austin, Austin, Texas 78712

D. Caleb Sargent<sup>‡</sup>

Sikorsky Aircraft, Stratford, Connecticut 06615

Daniel Shannon§

United Technologies Research Center, East Hartford, Connecticut 06108

Jayant Sirohi<sup>¶</sup>

University of Texas at Austin, Austin, Texas 78712

and

Brian E. Wake\*\*

United Technologies Research Center, East Hartford, Connecticut 06108

DOI: 10.2514/1.C034008

Rotor blades experience very high centrifugal forces that can be used to pump air to the outboard region of the blade through an internal duct, which can be used for flow control. Analysis or design of such systems requires accurate prediction capability. To validate current Reynolds-averaged Navier-Stokes simulation methodologies, an experiment was performed using a rotating pipe, and simulation results were compared to the measured data. A quasi-one-dimensional code was also compared to experiment as a lower-order simulation tool for faster solutions. The test and simulations include several combinations of steady inlet and exit conditions as well as an unsteady inlet valve operation at several rotational speeds. The quasi-one-dimensional code showed good correlation for steady inlet and exit conditions with boundary conditions obtained from experiment. Navier-Stokes methods also showed good agreement with measured data for pressure and mass flow rate at most conditions, while properly capturing complex flow features including separation, secondary swirl flow, and tip-flow interactions. The kinetic-eddy simulation and the Spalart-Allmaras turbulence models were tested to examine solution sensitivity under the complex flow environment. The two turbulence models showed similar results, except when the inlet valve was closed, in which case the kinetic-eddy simulation model showed better correlation.

# Nomenclature

valve area =

maximum valve area  $A_{\text{max}}$ = reference speed of sound =

duct diameter CF centrifugal force L reference length M Mach number

= mass m P pressure

 $P_{\text{ref}}$ reference pressure

duct radius

radial location  $R_{\rm inlet}$ intake radius temperature

reference temperature

delta quantity azimuth angle Ψ Ω = vorticity angular velocity

# I. Introduction

S THE demand for higher speeds, improved maneuverability, and more efficient rotorcraft increases, active and/or passive flow control technologies to suppress adverse flow effects due to retreating blade stall are receiving increased interest. For example, airfoil and blade planform shape modification or active control devices such as Miniature Trailing-edge Effectors [1], trailing-edge flaps [2], leadingedge slats, vortex generators, active twist control [3], and active flow control [4] have all been pursued in recent years. For most of these devices, first-principles-based computational fluid dynamics (CFD) simulations have been performed to evaluate the effect of these moving aerodynamic surfaces. Of particular interest for the current study are centrifugally powered internal flow concepts. Rotor blades experience very high centrifugal forces (CFs) with enough energy to provide effective pumping of the air within blade ducts. When an inboard inlet and outboard orifices are combined, it is possible to move large amounts of air through the blade to the outer portions of the blade where flow control is most effective. One example of a practical utilization of this effect is described in [5] in which tip blowing was used to modify the structure of the tip vortex and reduce rotor brownout. Other examples with internal flow control under high CF

Received 6 May 2016; revision received 5 August 2016; accepted for publication 19 August 2016; published online 28 November 2016. Copyright © 2016 by the authors. Published by the American Institute of Aeronautics and Astronautics, Inc., with permission. All requests for copying and permission to reprint should be submitted to CCC at www.copyright.com; employ the ISSN 0021-8669 (print) or 1533-3868 (online) to initiate your request. See also AIAA Rights and Permissions www.aiaa.org/randp

<sup>\*</sup>Staff Research Scientist, Department of Thermal and Fluid Sciences, 411 Silver Lane, MS 129-89. Member AIAA.

Graduate Research Assistant, Department of Aerospace Engineering and Engineering Mechanics, 210 East 24th Street. Member AIAA.

Senior Research Engineer, Engineering-Aeromechanics, 6900 Main Street, Member AIAA.

<sup>§</sup>Staff Research Engineer, Department of Thermal and Fluid Sciences, 411 Silver Lane, MS 129-89. Member AIAA.

Associate Professor, Department of Aerospace Engineering and Engineering Mechanics, 210 East 24th Street. Member AIAA.

<sup>\*\*</sup>Technical Fellow, Department of Thermal and Fluid Sciences, 411 Silver Lane, MS 129-89. Associate Fellow AIAA.

environment include the Sikorsky X-wing [6] and the tip jet-driven Boeing Canard Rotor Wing [7].

The ability to accurately predict time-varying pressures and mass flows is important for centrifugally powered flow control devices. Despite its relative simplicity as a blowing concept, modeling CF blowing introduces significant numerical challenges. The numerical method must predict the unsteady passive flow rate resulting from centrifugal effects and boundary conditions, which include external and internal flow losses (skin friction and viscous turning/mixing). The flow can be very complex, especially near the inlet and exit regions where the internal and external flow interact and mix. Additionally, because some implementations of CF blowing require a specific exit flow schedule to target particular rotor azimuth positions, a time-varying flow control valve may be required. The internal flow passage may also include bends and vanes at the inlet and outlet locations, which can introduce unsteadiness and flow separation. Furthermore, the coupling of the rotational blade motions and elastic deformations with the external flow further complicates the analysis.

To explore CF blowing concepts, collaboration between Sikorsky Aircraft Corporation, United Technologies Research Center (UTRC), and the University of Texas at Austin (UTA) was established with the goal of validating both a state-of-art CFD method as well as a lower-order quasi-one-dimensional (Q1-D) model against experimental data at relevant rotor blade operating conditions. The experiment was performed at UTA using a rotating pipe to represent a simplified ducted blade. Pressure and mass flow rate measurements are compared to predictions at several inlet and outlet conditions (open or closed) as well as for an unsteady inlet valve case. This study also shows sensitivities to turbulence models and examines the flow inside the pipe. Finally, potential issues regarding ducted blade simulation are identified.



Fig. 1 Duct test article mounted on rotor test stand.

# II. Experimental Setup and Measurement

The goal of this study was to measure internal flow quantities in a rotating duct so as to provide validation data for two numerical models described in the next section. The UTA CF blowing test rig is shown in Fig. 1. The test article is mounted on a rotor test stand powered by a hydraulic motor. It is composed of a rotating pipe attached at its midpoint to a central hub, with a bell-mouth inlet fixed to a nonrotating plate. One half of the pipe serves as the duct with centrifugally pumped flow, whereas the other half of the pipe serves as a counterweight (no internal flow). The hub and nonrotating plate comprise a valve at the root of the duct that is capable of varying the inlet cross-sectional area as a function of azimuth. The duct has a length of 52.75 in. with inner diameter of 2.07 in., rotating up to 1050 rpm. The open duct has a 90 deg turn to the bottom of the bellmouth inlet, which remains in the stationary frame of reference. The conditions of interest for this study include closed inlet-open exit, open inlet-closed exit, open inlet-open exit, and unsteady blowing with the root valve operating at various rotational speeds. CFD comparisons are made versus several internal duct static pressure sensors and mass flow rate measured at bell-mouth intake.

# A. Inlet Valve Configuration

A mechanical valve that opens and closes once per revolution was used to generate unsteady flow to determine how well the models capture these time-varying effects. Air enters the duct through a bellmouth intake (Fig. 2), which is attached to a nonrotating plate. As the hub rotates, a circular cutout on the nonrotating plate intersects a rectangular opening on the rotating hub such that the effective inlet area to the duct varies as a function of time. An elbow-shaped insert (inside the rotor hub) provides a smooth transition from the vertical to horizontal plane. Figure 3a shows the schematic of the top view of the assembly without the bell-mouth inlet. In this configuration, the valve is fully open as the circular cutout on the nonrotating plate is in contact with the rectangular slot corners on the hub. The size of the rectangular slot is chosen such that the inlet area (when fully open) is the same as duct cross-sectional area. As the duct rotates, the intersection of the circular and rectangular profiles produces an area profile that approximates a half of a twice-per-revolution sine wave (Fig. 3b).

# B. Instrumentation and Data Acquisition

Instrumentation consists of the four static pressure transducers (located spanwise at r/R = 0.25, 0.5, 0.75, 0.97), a six-component hub-mounted load cell, and a pitot rake to measure mass flow rate at the bell-mouth inlet. The static pressure transducers (Kulite LL-072) are based on piezoresistive Wheatstone bridges and have a full-scale range of 0–25 psia. The pressure transducers are mounted on the top of the duct such that the sensing diaphragm is parallel to the plane of

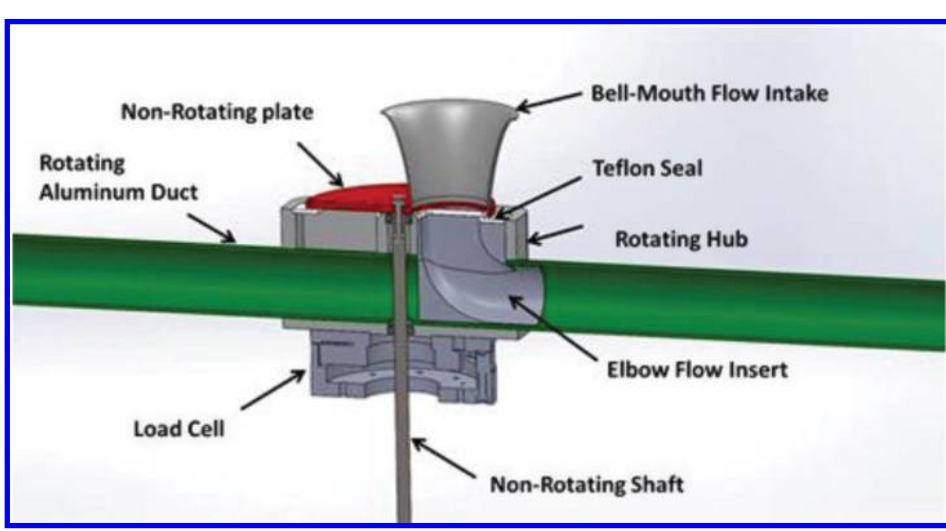
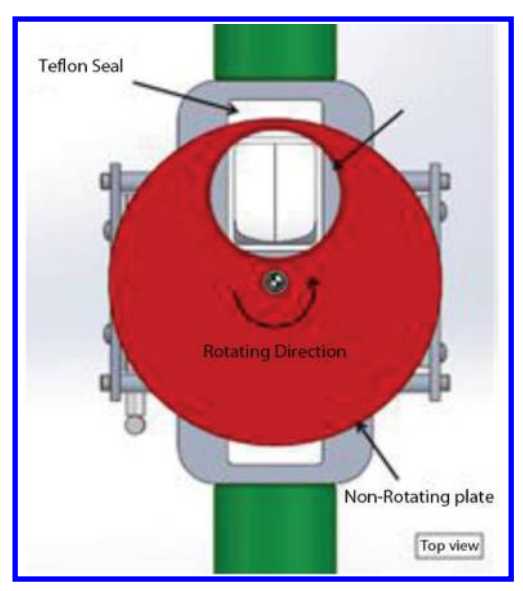
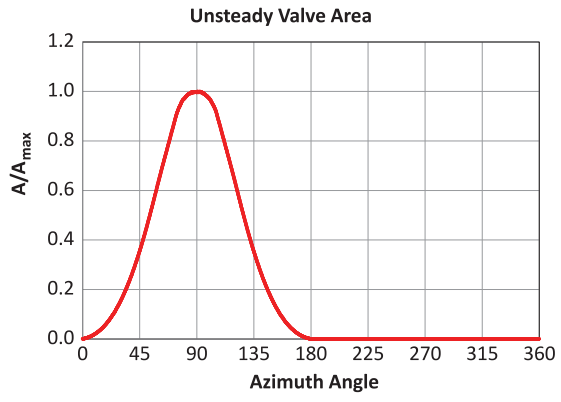


Fig. 2 Sectional view of the hub assembly. a) Schematic of inlet valve and b) unsteady inlet valve schedule of rotating duct.



a) Schematic of inlet valve



b) Unsteady inlet valve schedule of rotating duct

Fig. 3 Schematic of valve and opening schedule.

rotation. The pressure transducers were first calibrated on the bench top with a reference pressure sensor. One of the pressure transducers was then mounted in a sealed chamber and was separately tested by spinning to different rotational speeds to measure the effect of centrifugal acceleration. These tests revealed a centrifugal correction factor of  $7.5 \times 10^{-6}$  psig, that is, centrifugal correction factor multiplied by the centrifugal acceleration at the location of the pressure transducer must be subtracted from the measured pressure to

yield the correct pressure in the rotating frame. Signal conditioning and amplification of these transducers was performed by custom electronics on the rotor hub.

Mass flow rate of air through the duct is measured using a pitot rake consisting of three pitot tubes placed in the bell-mouth intake at cross-section locations ( $r/d=0.33,\ 0.5,\ 0.66$ ), where r is the radial distance from the inlet central axis, and d is the cross-sectional diameter of the intake. A differential pressure sensor (Endevco 8507C-1, full-scale 1 psi) is used to measure the pressure difference between the average total pressure and a wall static pressure port located in the same plane as the pitot rake. Flow velocities are quite low at the intake and are thus assumed to be incompressible. Only differential (total-static) pressure is used to calculate the flow velocity and mass flow rate.

A six-axis, strain-gauge-based load cell (ATI Omega 160) is used to measure the spanwise and chordwise forces as well as torque about the hub center in the rotating reference frame. The load cell is factory-calibrated with thrust and torque resolution of 0.17 lb and 0.0184 ft · lb, respectively, and typical accuracy of  $\pm 0.67$  lb and  $\pm 0.177$  ft · lb. The sensing range of the load cell is 0–1400 lb for spanwise and chordwise forces and 0–295 ft · lb for torque about the center of rotation.

### C. Test Procedure and Experimental Error

All data were recorded using two National Instruments PXI-6358 simultaneously sampled data acquisition boards at a sampling frequency of 30 kHz. At each rotational speed tested, 100 revolutions of data were acquired and phase-averaged using a once-per-revolution trigger signal generated by a Hall effect sensor. At least three test runs were performed at each rotational speed. The differential pressure signal from the mass flow rake was passed through a 300 Hz second-order Butterworth low-pass filter to eliminate frequency content due to acoustic response of the bell-mouth intake. Errors in the measurements are due to scatter from different test runs, centrifugal correction error (due to least-squares fit), electrical noise, and nonlinearity specified by the pressure transducer manufacturer. The scatter between test runs is the largest source of error (standard deviation ~0.019 psi), and this is plotted as error bars on the measurements.

# III. Analysis Methodologies

Numerical simulations were carried out with both low- and high-fidelity methods. The flow physics of a rotating duct or ducted blade is fully three-dimensional and includes complex interactions and mixing between the internal and external flows. Fully three-dimensional (3-D) Reynolds-averaged Navier–Stokes (RANS) simulations offer a method of predicting and examining these effects but require significant computational expense. Alternatively, the problem can be simplified and assumed as a quasi-one-dimensional (1-D) flow with prescribed boundary conditions at the inlet and

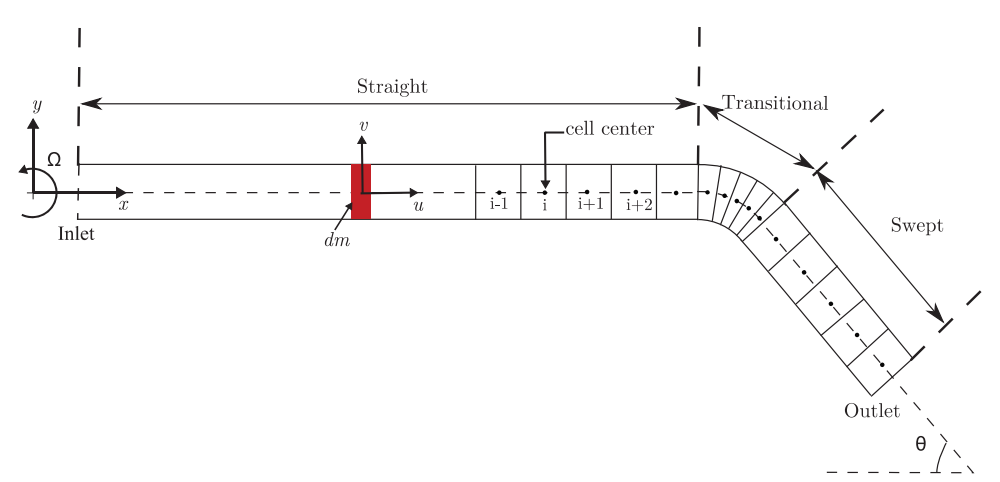


Fig. 4 Schematic of discretized rotating duct [8], a) Modeled geometry, b) grid system for bell-mouth inlet and duct (isometric view), and c) grid system for open inlet-closed exit (without bell-mouth inlet).

outlet. This approach does not capture the flow interaction and 3-D effects properly but provides data in a relatively short period of time, lending itself well to rapid design iterations. Both methodologies are compared to the experimental data in this paper.

# A. Low-Fidelity Quasi-One-Dimensional Euler Simulation

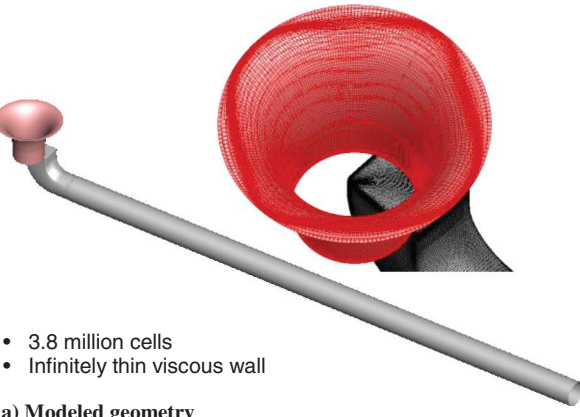
The low-fidelity method is a quasi-1-D Euler equation solver developed at UTA [8]. The model captures centrifugal and Coriolis effects, duct friction, sweep, and a time-varying duct cross section that simulates a flow control valve. The numerical methodology is termed "quasi-1-D" (Q1-D) because, although the Euler equations are formulated in 2-D, the duct is discretized only along its axis (1-D). The governing equations are written in the rotating frame. The Advection Upstream Splitting Method scheme, described by Liou and Steffen [9], is used to calculate the inviscid fluxes. Viscous effects are handled separately in the case of 1-D discretization by incorporating a duct friction factor defined using Churchill's approximation for turbulent flow [10]. Various boundary conditions, representing both closed and open-ended rotating ducts, are implemented using a combination of isentropic flow theory and Riemann invariants. For an open inlet, the flow is assumed to enter the duct with stagnation conditions. For a closed inlet, the velocity at the inlet face is set to zero. For a subsonic outlet, the pressure at the outlet is specified. In the supersonic outlet case, flow properties at the outlet face are extrapolated using a zeroth-order approximation. In the case of a closed outlet, the outlet velocity is set to zero. An explicit fourthorder Runge-Kutta scheme is used for time marching. Arbitrary opening and closing of a flow control valve in the duct is modeled as a local change in the duct cross-sectional area as a function of time. However, the current study shows simulations from steady open or closed valve positions only. A schematic of the discretized rotating duct reproduced from [8] is shown in Fig. 4. For more details of the solver, the reader is referred to [8].

#### B. High-Fidelity Reynolds-Averaged Navier-Stokes Simulation

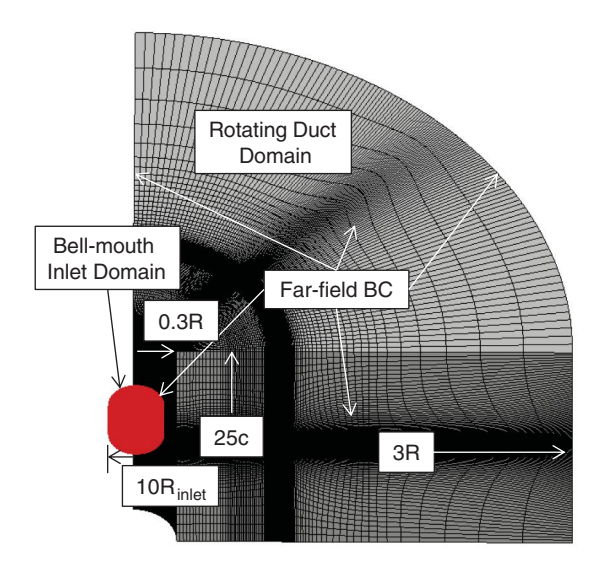
The high-fidelity method uses UT-GENCAS, a RANS solver developed at Georgia Tech [11] and further modified at UTRC. It is a generalized multiblock structured grid solver with second-order dual-time stepping method incorporating multigrid scheme for accelerated convergence. For spatial derivatives, Roe's Flux Difference Scheme with third-order Monotone Upstream-centered Scheme for Conservation Laws was used. Turbulence closure was achieved by two-equation kinetic-eddy simulation (KES) [12] or one-equation Spalart-Allmaras (SA) [13] model. The SA model included approximated rotational correction term [14]. The KES model was chosen based on a past validation study with UT-GENCAS for stalled airfoils and rotor simulation [15]. In the current study, both turbulence models were tested to examine solution sensitivity. Unless stated otherwise, the default turbulence model was the KES model.

The grid was generated by the topology-based grid generator Gridpro [16]. Figure 5 shows the computational grid consisting of a single duct and bell-mouth domain. A far-field characteristic-based in/outflow boundary condition was applied at all outer surfaces of both the rotating duct and the bell-mouth inlet domain. The duct domain and the inlet domain are not connected other than through the sliding inlet interface surface. It is assumed that the impact of disturbed flow in the rotating duct to bell-mouth domain is negligible. Likewise, it is also assumed that the induced flow around the bellmouth inlet has a minimal impact on the external flow surrounding the duct. It is also noted that early simulations with a 360 deg computational domain including both ducts showed minimal impact on the internal flow characteristics. Thus, to save computational time, only one quarter of the domain was used for the data presented herein. The bell-mouth domain is nonrotating for the unsteady valve simulation, but it was rotating with the duct for the closed-inlet-openexit, open-inlet-open-exit, and open-inlet-closed-exit conditions. The rotating duct computational domain extends between 0.3R and 3R in the spanwise direction and approximately 25 chords to top and bottom boundaries. The bell-mouth inlet domain extends to  $10R_{inlet}$  Bell-mouth domain:

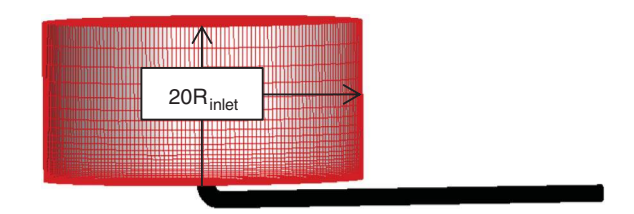
- · Nonrotating for unsteady valve model
- · Rotating for steady valve model



a) Modeled geometry



b) Grid system for bell-mouth inlet and duct (Isometric View)



c) Grid system for open inlet-closed exit (without bell-mouth inlet)

Fig. 5 Computational grid (BC, boundary condition).

around the inlet and  $20R_{inlet}$  in the vertical direction. The total cell count was 3.8 million, and the wall normal grid spacing was set to a y+ value less than 1. The duct and bell mouth were modeled as infinitely thin viscous walls. For the open-inlet-closed-exit case, the bell-mouth surface was removed, and the inlet domain was extended to  $20R_{\text{inlet}}$ . Also, only the internal duct was modeled with the tip surface blocked as a wall (Fig. 5c).

The unsteady valve operation at the interface between the nonrotating bell-mouth grid and the rotating duct grid was accomplished by switching between slip-wall and sliding interface boundary conditions, based on grid point alignment at a given rotational position. If boundary cells were aligned between the stationary and rotating domains, a sliding interface boundary condition was imposed. If they were misaligned, a slip-wall boundary condition was imposed.

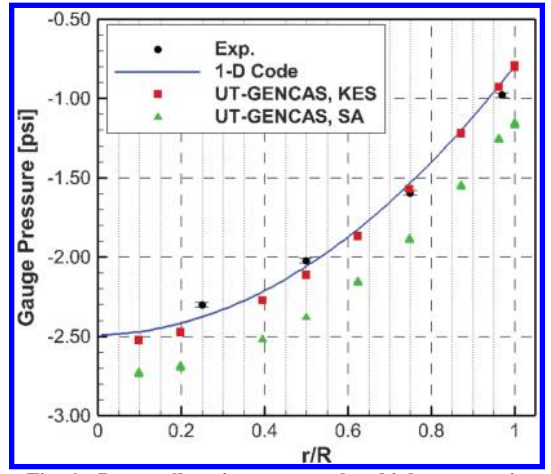


Fig. 6 Duct wall static pressure: closed inlet-open exit.

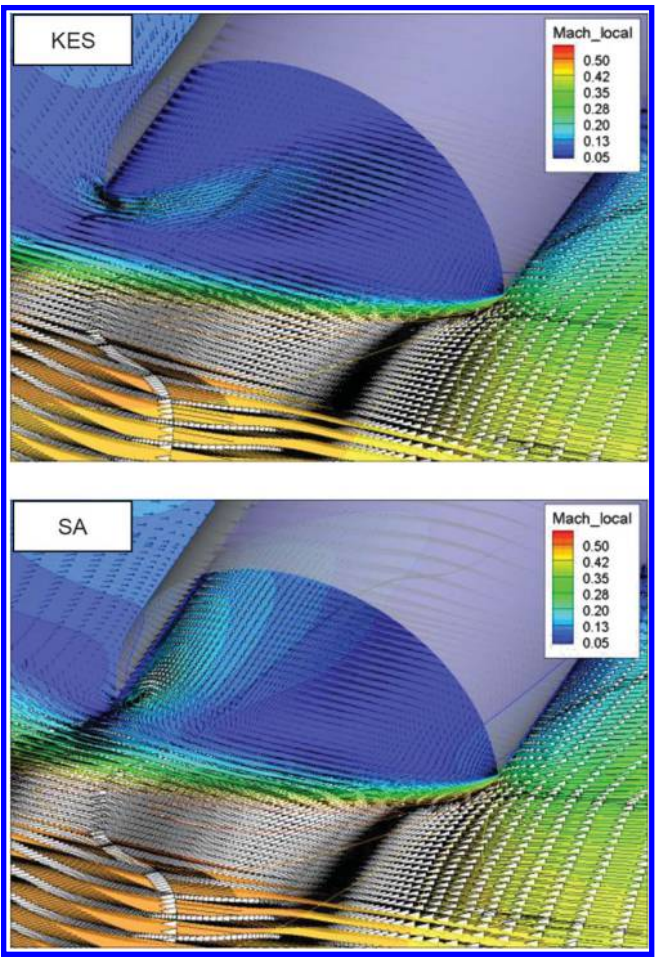


Fig. 7 Mach contour: closed inlet-open exit.

For all simulations, 100–150 subiterations were used with a multigrid scheme to ensure convergence. All simulations were performed in unsteady mode with 0.1 deg of rotation per time step. The solution was found to converge in three revolutions for unsteady inlet valve operation cases and less than two revolutions for steady inlet position cases (excepting the open-inlet–closed-exit case, which will be addressed later). This study focuses primarily on a high 1050 rpm case with a tip Mach number of 0.43, which corresponds to the upper limit of the UTA test stand hub-mounted load cell torque sensing range. Additional cases were run at 800 and 400 rpm to examine correlation sensitivity. The primary metric of interest is the mass flow rate because it is the most important performance parameter for rotorcraft flow control applications. Also shown for

correlation purposes is the local static wall pressure at several radial locations as measured in the UTA test rig.

#### IV. Results and Discussion

# A. Closed Inlet-Open Exit

The closed-inlet-open-exit condition was run at 1050 rpm, tip Mach number of 0.43, and tip Reynolds number based on duct diameter of 0.53M. In the experiment, the bell-mouth inlet was removed, and the inlet surface of the duct was sealed. In the simulation, the bell-mouth inlet domain was maintained, but the duct inlet surface was always set to slip-wall boundary condition. The mass flow rate is zero in this case. The duct is working as a vacuum pump and generates a low pressure at the inboard section of the duct. Figure 6 compares the measured duct wall static (gauge) pressure with the Q1-D and two RANS simulations. The Q1-D code inlet boundary condition was set as a hard wall, and the tip pressure condition was set by extrapolating the duct wall static pressure measured at 0.97R to the tip. The centrifugal force is linear with radial distance (CF =  $m\omega^2 r$ ), and the radial pressure distribution is expected to be quadratic in nature. The shape and value of the pressure distribution agrees very well with all methods except the SA RANS simulation. The difference between the KES and SA models is approximately a constant offset of 0.2 psi, which is about 1.3% of the absolute pressure. The shape of the SA predicted pressure distribution is very similar to the KES and Q1-D code, but shifted to a lower tip pressure. Figures 7 and 8 compare two solutions around the duct tip with Mach and pressure contours respectively (external flow is incident on the duct tip from right to left). The SA model shows less deflection of the leading-edge flow disturbance that interacts with the inner trailing edge of the duct. Conversely, the KES model shows a wider turn around the leading edge that facilitates some recirculation of the flow around the trailing edge. As a result, the SA model shows

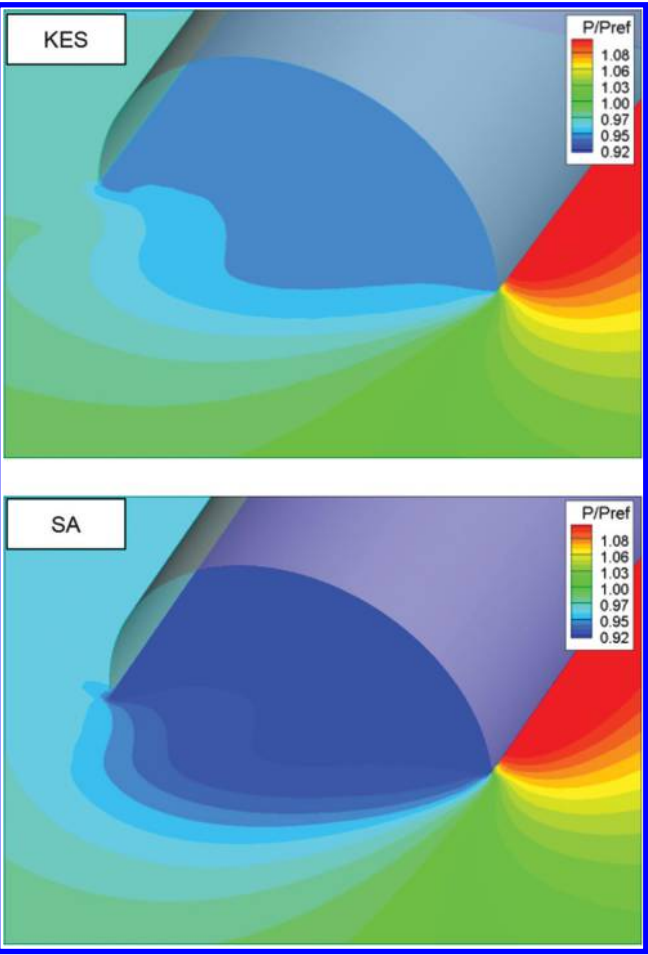


Fig. 8 Pressure: closed inlet-open exit.

lower pressure inside the duct around the tip than the KES model, which results in lower internal pressures throughout the duct.

# B. Open Inlet-Open Exit

In the open-inlet-open-exit condition, the centrifugal force drives steady flow through the rotating duct. The RANS simulation was performed with the bell-mouth inlet fully aligned and rotating with the duct inlet (thus, fully opened). Figure 9 compares gauge pressure from the simulations to the experimental data. The peak pressure drop was about half of the closed-inlet-open-exit condition. Both RANS simulations underpredicted the pressure drop compared to the measurement, although the SA model shows slightly better correlation. The underprediction is consistent across the span, and the quadratic trend is in good agreement with measurement and the Q1-D code. The experiment and RANS simulations show tip pressures higher than ambient pressure due to the mixing of the internal external flows at the tip. It is noted again that the Q1-D code used the tip boundary condition extrapolated from measurement; thus, it follows that the Q1-D code agrees well with measurement near the duct tip. If RANS data are used for the boundary condition, it was confirmed that the Q1-D code agrees very well with RANS simulation, indicating that the Q1-D code is sensitive to the prescribed boundary conditions. It also indicates that the internal pressure distribution depends on tip pressure, and error in tip pressure prediction contributes to internal pressure discrepancies.

The sudden pressure drop seen at  $\sim 0.1R$  in the RANS simulation is due to the 90 deg turn, which is not modeled in the Q1-D simulation.

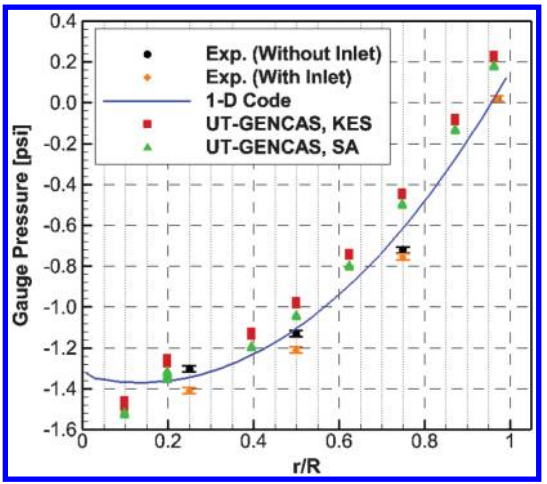


Fig. 9 Duct wall static pressure: open inlet-open exit.

Figure 10 shows complex flow features around the inlet. A recirculation zone is developed where the flow turns from circular bellmouth inlet to the rectangular duct inlet. As flow makes a 90 deg turn following the duct, separation is formed at the upper surface corner. The presence of a strong secondary swirl flow is also apparent. This is typical of turning pipe flows due to the internal pressure gradient around the turn. The secondary swirl flow is known to be one of major flow loss mechanisms [17]. Figures 11a and 11b show flows around tip with horizontal and vertical cut-planes illustrating pressure and Mach number contours, respectively. The flow at the tip includes duct flow mixing with external flow. The duct flow is skewed backward due to external flow, and a high-pressure region is formed around exit plane. At the top and bottom of the duct, the pressure suction due to the accelerated flow over the cylinder surface induces vortex roll-up. All these flow features add complexity, and the RANS simulations may be subject to error, especially with separation and mixing, which are known to be challenging for RANS simulations. Another source of error is the duct thickness. The RANS model has zero thickness, encouraging exit flow more tangential than a real duct with finite thickness. Even with the flow complexity and potential sources of error, the correlation between RANS simulations and measurement can be seen as good agreement. The difference between two turbulence models is less than 0.1 psi, and the difference between the KES model and measurement around the tip is about 0.2 psi (~1.3% of absolute pressure). Table 1 summarizes the predicted and measured mass flow rates. The measured data are from rake installed inside the bell-mouth inlet. The experiment showed about 10% more mass flow rate as a result of lower tip pressure compared to simulations.

# C. Open Inlet-Closed Exit

For the open-inlet-closed-exit condition, the net mass flow rate becomes zero, and the flow is compressed toward the tip with the pressure gradient balancing the centrifugal force. Despite the steady nature of this case, it was found to be the most challenging simulation in terms of convergence. The flow velocity becomes nearly zero, which can create convergence difficulties in density-based compressible flow solvers. Another reason is that the only way the initial numerical error inside the duct can be washed out is through the small duct inlet with very low transient flow velocities. Thus, this case took the most simulation time in comparison to the other cases. Figure 12 shows the pressure convergence history at several radial locations. The simulation was carried out without the bell-mouth inlet (Fig. 5c) and the duct rotating at 1050 rpm. The KES turbulence model was used for this case. The domain was initialized with zero velocity and ambient pressure, as if the duct was at rest. Then, it was immediately rotated to 1050 rpm. Thus, the transient solution includes both numerical and physical phenomena. Once the standing

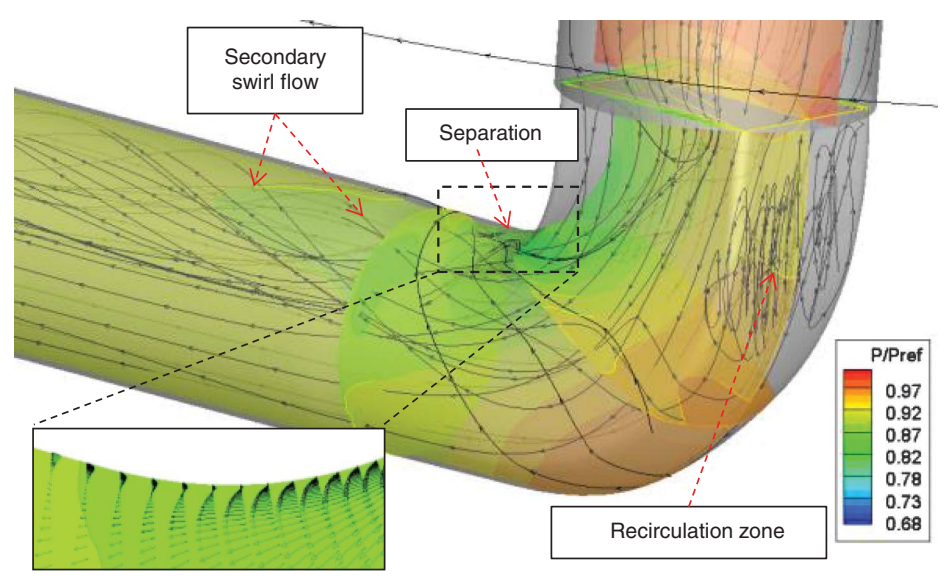


Fig. 10 Flow around inlet: open inlet-open exit. a) Pressure contour b) Mach contour.

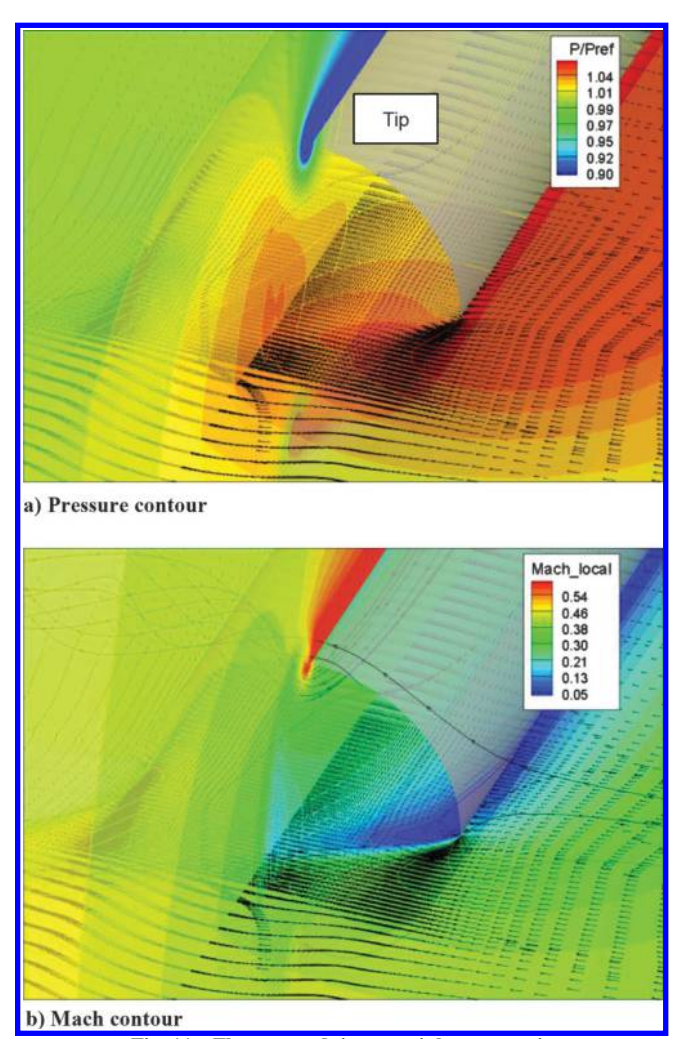


Fig. 11 Flow around tip: open inlet-open exit.

flow is suddenly rotated, the flow inside duct experiences fluctuation until it settles with balanced pressure and centrifugal force. To reduce the computational time, the simulation began with 30 subiterations without multigrid. After two revolutions, the multigrid scheme was turned on to increase subiteration convergence, and the pressure fluctuation was greatly reduced with increased fluctuation frequency. After three revolutions, the number of subiteration was increased to 100, and this resulted in a noticeably smoothed wave form with slightly increased fluctuation frequency. After four revolutions, the number of subiterations was increased to 150 with little change in the convergence trend. The simulation was stopped after six revolutions. Figure 13 shows mass flow rate convergence history at several radial locations. The negative mass flow rate indicates flow directed toward the duct root. The similar convergence trend change is observed based on numerical setting event. Thus, the change in the convergence trend after each parameter setting event is numerical. A preconditioning may accelerate subiteration convergence with the multigrid scheme. A simulation with approximated initial pressure distribution may also reduce convergence time.

Figure 14 compares simulated pressure distributions to the measured data. In this case, the KES model was used, and the last revolution of data was averaged after six revolutions. The quadratic

Table 1 Mass flow rate: open inlet-open exit

	Mass flow rate,	Percent
Method	slug/s	difference, %
Experiment (with bell-mouth inlet)	0.0177	
UT-GENCAS, KES	0.0158	11
UT-GENCAS, SA	0.0162	8.5

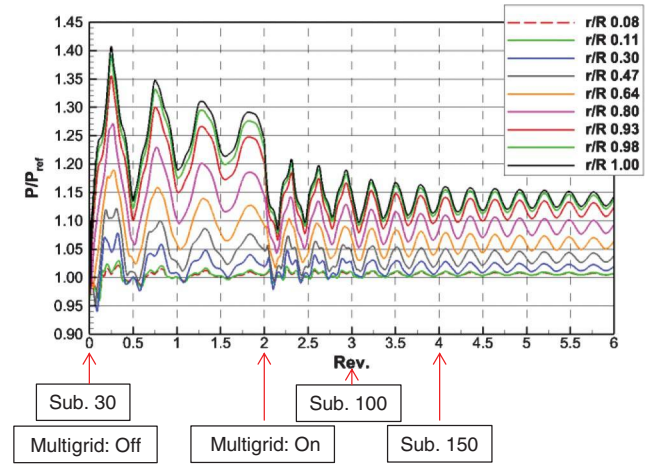


Fig. 12 Pressure history: open inlet-closed exit.

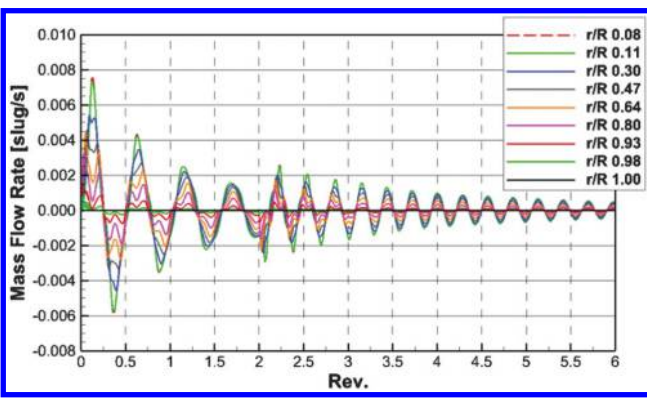


Fig. 13 Mass flow rate history: open inlet-closed exit.

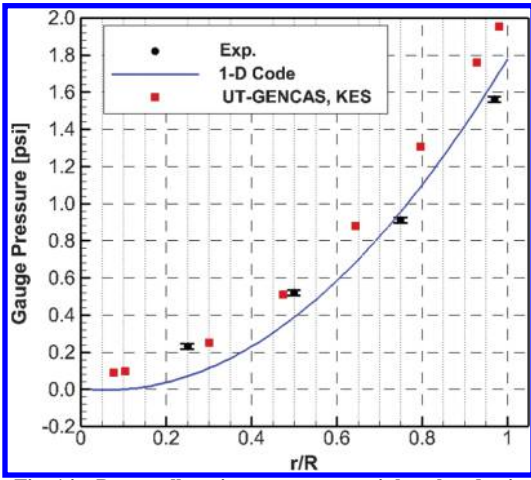


Fig. 14 Duct wall static pressure: open inlet-closed exit.

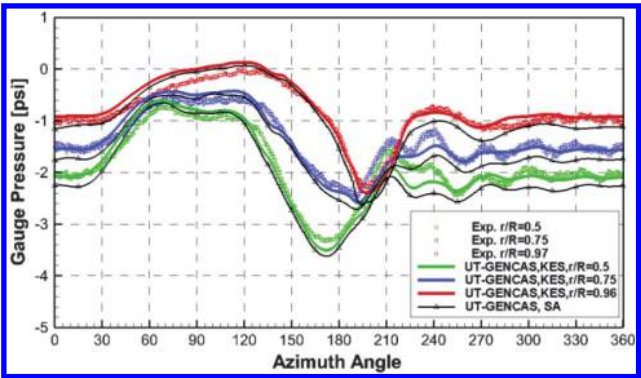
shape of the pressure distributions for the UT-GENCAS and Q1-D simulations are quite similar, but the UT-GENCAS has a slightly higher inlet pressure. The Q1-D code used an ambient pressure assumption at the inlet boundary. The measured pressure was close to the UT-GENCAS simulation at the inboard region but slightly lower beyond 0.5*R*. It is not clear what caused the difference for this case. Potential contributors could be simulation errors due to decoupled external duct from the inlet domain or measurement uncertainty including CF corrections, flow leakage at the tip, etc.

# D. Unsteady Valve Motion

To simulate valve operation, the nonrotating bell-mouth inlet was installed on top of a nonrotating plate as described in Sec. II. The inlet

of the rotating duct and the bottom area of the bell-mouth inlet were designed such that the inlet opening area goes from fully closed to fully open in a quarter of a revolution and then closes again in a quarter revolution, as shown in Fig. 3b. In this unsteady valve operation test, three rotor speeds were simulated to validate the RANS model and to examine correlation sensitivity. The azimuth angle was defined such that the maximum valve opening occurs at 90 deg. The Q1-D code simulation was not included because of uncertainty in the tip pressure and impedance boundary condition. The unsteady flow excited numerical and acoustic oscillations in the Q1-D model that were not realistic to either the RANS simulation or the measured data; these oscillations persisted due to the inviscid treatment of the Q1-D model. The three rotation frequencies tested were 1050, 800, and 400 rpm, with corresponding tip Mach numbers of 0.43, 0.33, and 0.16 and tip Reynolds numbers of 0.53 million, 0.4 million, and 0.2 million, respectively. Time histories of the internal duct pressure at 0.5R, 0.75R, and 0.97R and the mass flow rate measured in the bell-mouth inlet are compared.

Figures 15-17 compare the pressure history at each value of rotation frequency. The KES model was used at all conditions, and the SA model was tested at 1050 rpm to examine solution sensitivity. At all rotation frequency conditions, the KES RANS simulations



Pressure history: unsteady valve, 1050 rpm.

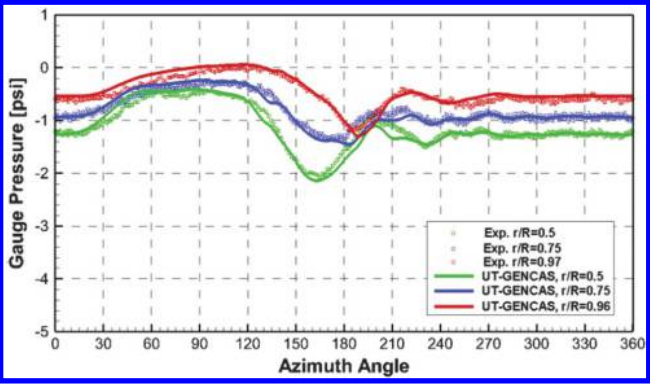


Fig. 16 Pressure history: unsteady valve, 800 rpm.

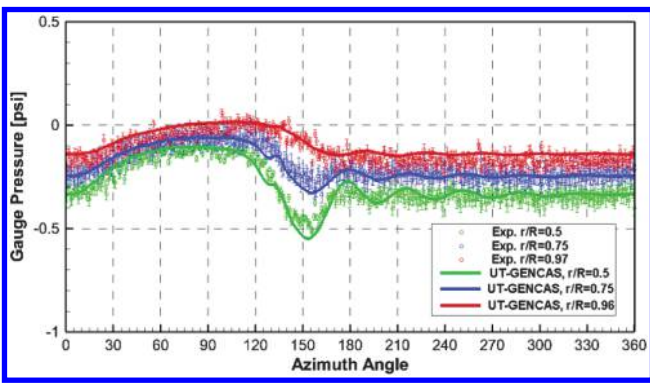


Fig. 17 Pressure history: unsteady valve, 400 rpm.

show good correlation with the measured data. A pressure wave traveling at the speed of sound under standard ambient conditions (~1116 ft/s) would take approximately 25 deg at 1050 rpm, 19 deg at 800 rpm, and 9 deg at 400 rpm to travel from the root to the tip. The initial pressure rise in the RANS simulations near the tip properly reflects these acoustic time scales. It should be noted that the experimental data showed an approximately 8 deg phase shift in the pressure histories, which has been corrected. The correction was based on theoretical wave propagation speed as noted previously. This is most likely due to a signal triggering delay in the experiment. The peak pressure drop at around 180 deg and following recovery all match very well with experiment, with slightly lower pressure recovery predictions at 1050 rpm at the inboard stations. The reflected waves after valve closure were also captured well, but the predicted pressure near the tip shows more dissipation and a loweramplitude waveform. Despite these differences, most of the pressure results from the KES RANS simulation were within the measurement error for all rotation frequency conditions. The SA model also shows good agreement with the 1050 rpm unsteady flow case, but it shows slightly lower pressures when the valve is closed. This finding is consistent with the earlier closed-inlet-open-exit condition.

Figures 18-20 compare predicted and measured mass flow rates for each value of rotation frequency. The thickness of the

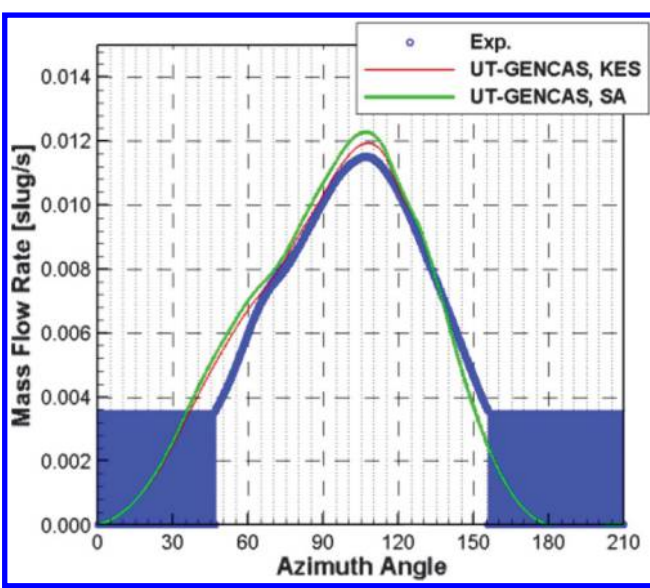


Fig. 18 Mass flow rate: unsteady valve, 1050 rpm.

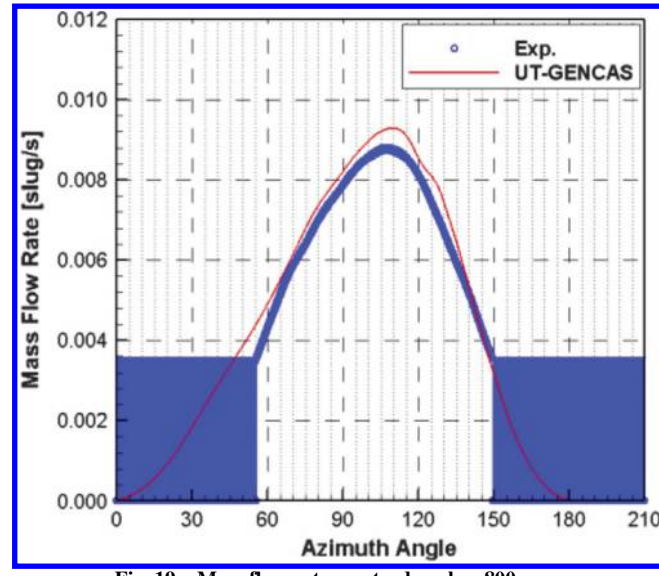


Fig. 19 Mass flow rate: unsteady valve, 800 rpm.

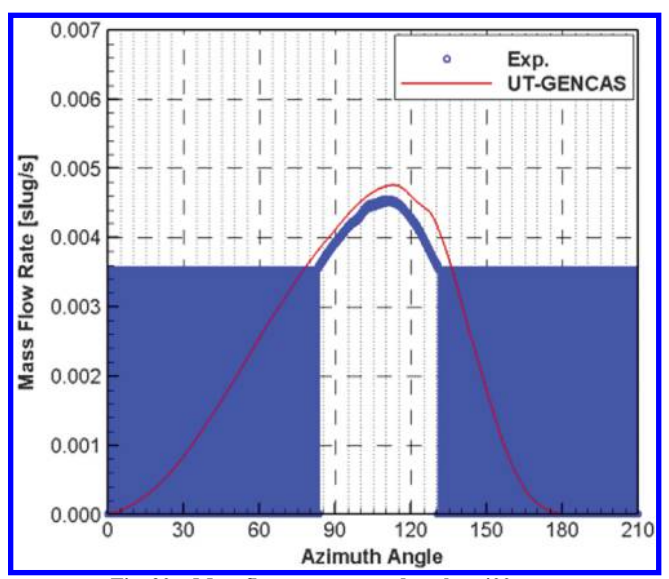


Fig. 20 Mass flow rate: unsteady valve, 400 rpm.

measurement line represents the error bound. The large measurement error at low flow rates arises due to propagating the uncertainty in the differential pressure transducer, which is dominated by its noise floor at zero rotational speed. The SA model is shown only for 1050 rpm. The peak mass flow rate occurs around 110 deg, after passing the maximum valve opening at 90 deg. The RANS model predicts the shape and amplitude of the mass flow profile at all values of rotation frequency with a slight overprediction of the peak value. The overprediction is higher with the SA model. The sudden slope change around 70 deg at 1050 rpm is also captured by the prediction.

Figure 21 shows the flow features with Mach contours and streamlines around the inlet at several azimuth locations for the 1050 rpm unsteady flow case. As the valve starts to open, flow is

sucked into the low-pressure duct (due to aforementioned closedinlet-open-exit vacuum effect). Recirculation zones form around the inlet, where the flow turns from bell-mouth inlet to the rectangular elbow insert, and the flow accelerates through the outer radius of the duct bend. The inner radius region remains at a relatively low pressure, and secondary swirl flow structures develop due to the radial pressure gradient. These relatively strong secondary swirl features have chordwise flow vectors. It is possible that the development of this secondary flow between 60 and 90 deg azimuth may be responsible for the inflection point in the mass flow rate slope at these angles. The flow rate continues to increase after passing 90 deg until the mass flow rate peaks at a lower value than was observed for the open inlet-open exit. This suggests that the valve schedule is too short in comparison to the flow response times to reach the maximum potential mass flow rate. This response time may be a factor of the scale of the test rig and should be explored further to assess its impact on full-scale rotor flow control applications.

Figure 22 shows similar flow features at 800 rpm. Relative to the flow at 120 deg (before the mass flow rate inflection point), the flow at 130 deg (in the middle of mass flow rate bump) shows a higher Mach number surrounding the low-speed swirl flow area at the radial cut plane, after the turn, even with the expanded recirculation zone seen from the cut plane in the middle of the turn.

The duct flow properties were studied in more detail for the 1050 rpm case with the KES turbulence model. Figures 23–26 show section-averaged pressure, temperature, mass flow rate, and vorticity magnitude at several radial stations. The section-averaged pressure (Fig. 23) shows how the rising pressure wave propagates from root to tip. The wave amplitude is damped as it propagates outboard. The temperature history (Fig. 24) shows a peak fluctuation in amplitude of 55°F at 0.3*R*. The temperature increases as the valve is opened and drops when the valve is closed because of the vacuum pumping effect. The short time period of fluctuation (90 deg in the current case) may not be significant for duct structural properties. However, if a test is performed with inboard section instrumentation, which requires temperature for data reduction, this temperature fluctuation should be properly accounted for. The mass flow rate history (Fig. 25) shows an

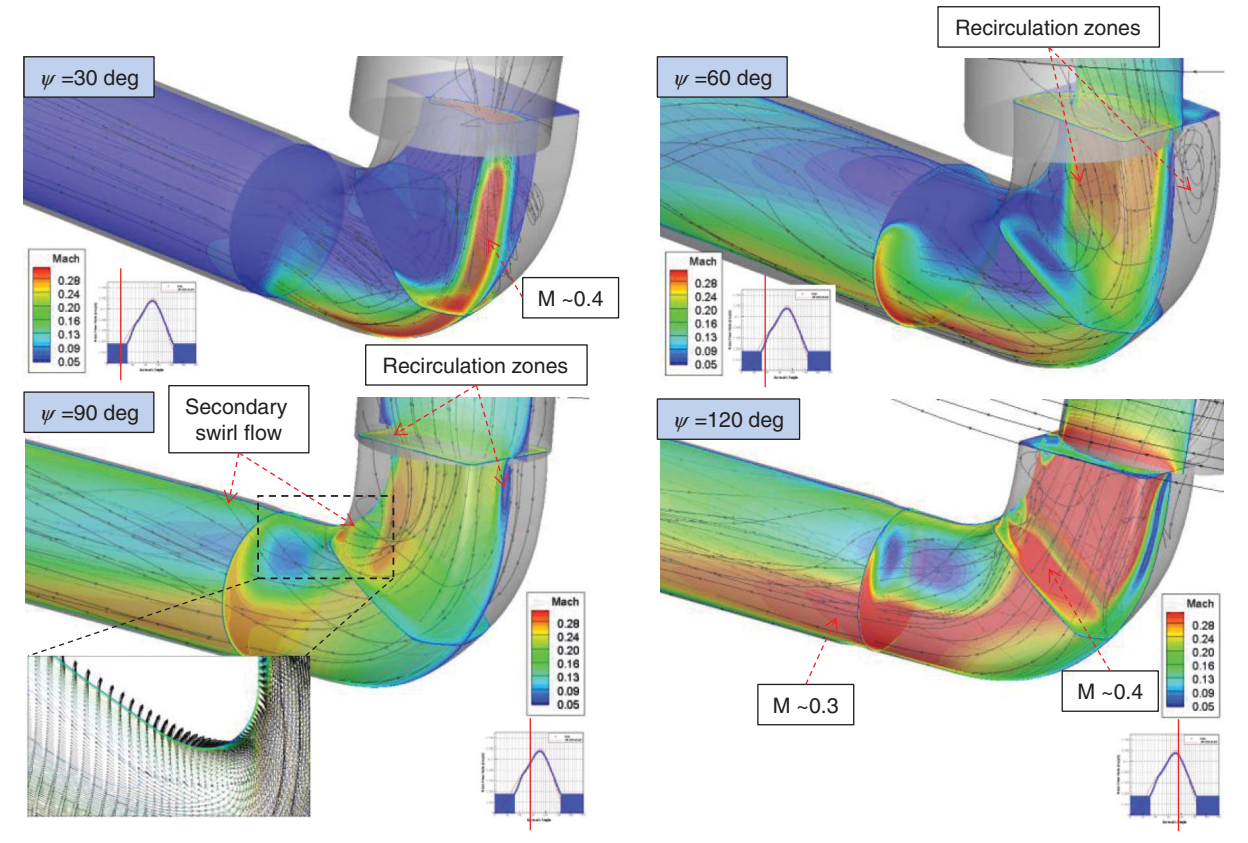


Fig. 21 Flow features, unsteady valve, 1050 rpm.

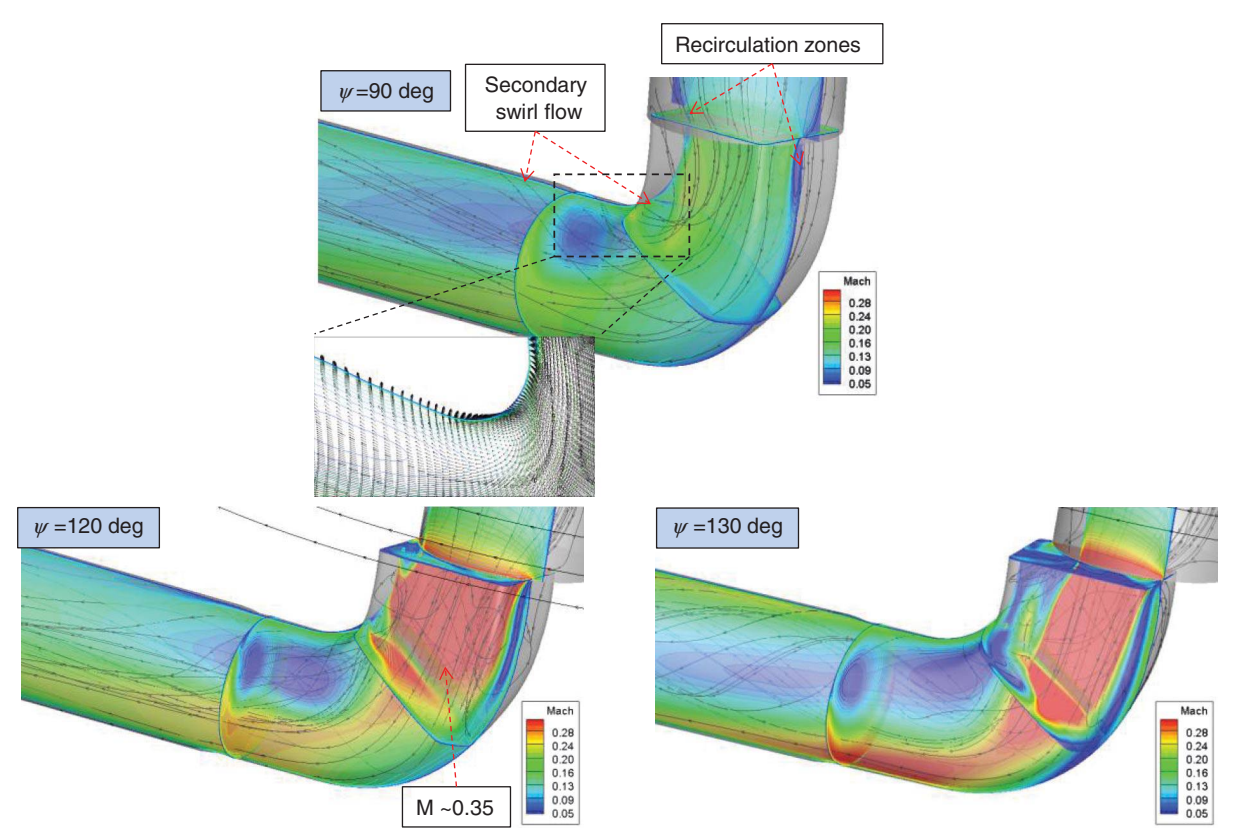


Fig. 22 Flow features, unsteady valve, 800 rpm.

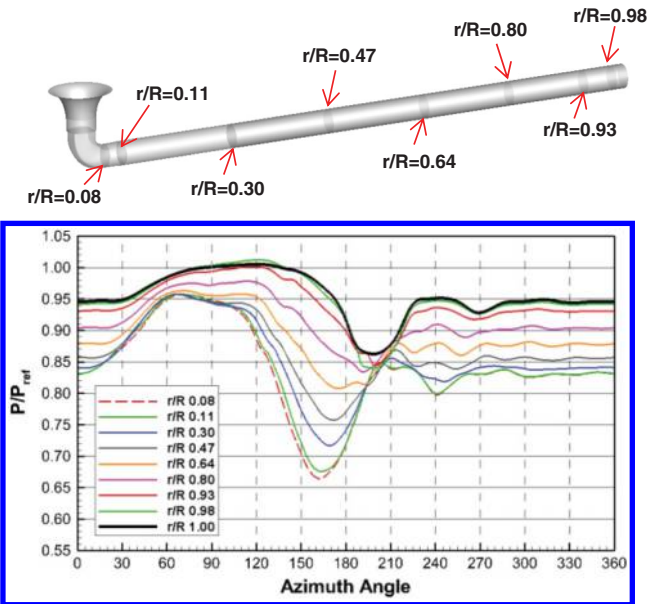


Fig. 23 Section-averaged pressure, 1050 rpm.

oscillating flow after the valve is closed at 180 deg. A change in flow direction occurs just as the valve closes due to a momentum imbalance at the root. Several reflected waves are then observed as the disturbance oscillates between the tip and the root, with the flow finally settling just before the next valve opening event.

The vorticity magnitude history (Fig. 26) shows elevated vorticity at the inboard sections when the valve is opened. This increased vorticity is due to separation and secondary swirl flow through the 90 deg turn. The high vorticity near the tip after the valve is closed occurs when the mass flow rate is very low or slightly negative. This results in some recirculation near the tip trailing edge and an increase in vorticity, similar to what was shown in Fig. 7. It is noticed that the

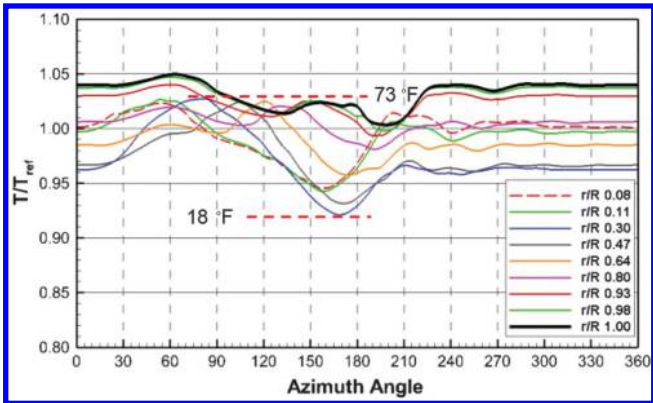


Fig. 24 Section-averaged temperature, 1050 rpm.

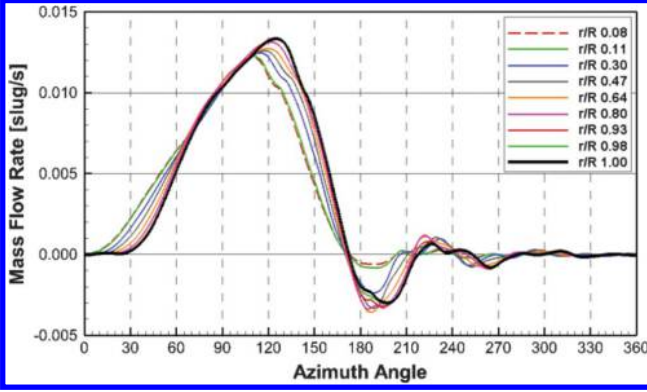


Fig. 25 Section-averaged mass flow rate, 1050 rpm.

high inboard section vorticities are not well conserved along the duct. Although viscous diffusion with chordwise Coriolis force contributes to this, it could be largely due to numerical dissipation. A potential

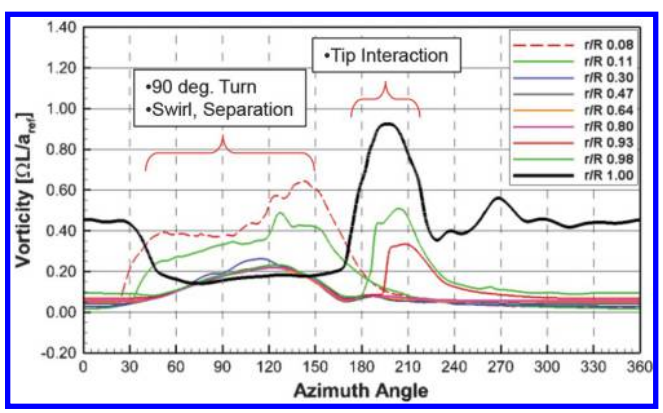


Fig. 26 Section-averaged vorticity, 1050 rpm.

result of this numerical dissipation is a reduction in wave shape conservation and a resultant reduction in internal/external flow interaction strength. A refined mesh or higher-order scheme may be used to better resolve this interaction.

#### V. Conclusions

The goal of this effort was to validate numerical tools for the simulation of centrifugally driven flow inside a rotor blade for flow control applications. A scaled rotating duct with unsteady valve motions was tested, and numerical simulations were compared against test data. The primary comparison parameters were static internal wall pressure and mass flow rate. Several inlet and tip conditions were tested experimentally and numerically. These include closed-inlet-open-exit, open-inlet-open-exit, open-inlet-closed-exit, and unsteady valve operation at several rotational speeds. Numerical simulations include a quasi-steady 1-D code and RANS code (UT-GENCAS) with a twoequation kinetic-eddy simulation (KES) and a one-equation SA turbulence models. The unsteady valve simulation was successfully performed using a sliding interface between a nonrotating bell-mouth inlet domain and a rotating duct domain. Overall, the validation showed good correlation between test data and UT-GENCAS. The primary physics were captured properly, and the predictions were reasonably close to the measured data. The RANS simulation shows major flow features including separation around the inlet, secondary swirl flow induced by the 90 deg inlet turn, and flow interaction around the tip. All these features are potential sources of total pressure loss and mass flow rate deterioration. Thus, it is important to capture these flow features accurately. The simulation shows sensitivity to the turbulence model as it affects these major flow features. It appears that the KES model performs better for these specific cases, although the difference was relatively small in the unsteady case. The major difference between the turbulence models stems from tip flow interaction when the inlet valve was closed. In this scenario, the SA model predicts a lower pressure distribution. The open-inlet-closed-exit condition presents a significant numeral challenge with respect to convergence. Fast subiteration convergence schemes (such as multigrid and preconditioning) are recommended to improve numerical convergence. The vorticity magnitude history shows considerable numerical dissipation from inboard to outboard. It is recommended that a finer mesh and higher-order schemes for simulations be used to more accurately capture these flow phenomenon. The quasi-steady 1-D code also showed good agreement with test data for steady valve cases with prescribed end surface boundary condition from the experiment, validating that the Q1-D code is a viable tool to use in design iterations.

More advanced turbulence models, a more accurate geometry representation that includes pipe wall thickness, and a computational domain that surrounds the entire experimental setup may be explored for further improved correlation.

# Acknowledgment

This research was partially funded by the Government under agreement W911W6-11-2-0001. The U.S. Government is authorized to reproduce and distribute reprints for Government purposes notwithstanding any copyright notation thereon.

#### References

- [1] Matalanis, C. G., Wake, B. E., Opoku, D., Min, B. Y., Yeshala, N., and Sankar, L. N., "Aerodynamic Evaluation of Miniature Trailing-Edge Effectors for Active Rotor Control," *Journal of Aircraft*, Vol. 48, No. 3, May–June 2011, pp. 995–1004. doi:10.2514/1.C031191
- [2] Depailler, G., and Friedmann, P. P., "Reduction of Vibration Due to Dynamic Stall in Helicopters Using an Actively Controlled Flap," 43rd AIAA/ASME/ASCE/AHS/ASC Structural Dynamics, and Materials Conference, AIAA Paper 2002-1431, April 2002.
- [3] Brouwers, E. W., Zientek, T. A., and Centolanza, L. R., "Twist Effects on Rotor Performance, Loads and Vibrations," *Proceedings of the 71st Annual Forum of the American Helicopter Society* [CD-ROM], AHS International, Alexandria, VA, May 2015.
- [4] Matalanis, C. G., Min, B. Y., Bowles, P. O., Jee, S., Wake, B. E., Crittenden, T. M., Woo, G., and Glezer, A., "Combustion-Powered Actuation for Dynamic-Stall Suppression: High-Mach Simulations and Low-Mach Experiments," *AIAA Journal*, Vol. 53, No. 8, 2015, pp. 2151–2163. doi:10.2514/1.J053641
- [5] Kuerbitz, D., and Milluzzo, J., "Investigation of Centrifugal Pumping Rotor Blades as a Means of Vortex Diffusion," *Proceedings of the 71st Annual Forum of the American Helicopter Society* [CD-ROM], AHS International, Alexandria, VA, May 2015.
- [6] Krauss, T. A., and Kingston, L., "X-Wing Aircraft Circulation Control," U.S. Patent 4,573,871, 1986.
- [7] Mitchell, C. A., and Vogel, B. J., "The Canard Rotor Wing (CRW) Aircraft—A New Way to Fly," AIAA International Air and Space Symposium and Exposition: The Next 100 Years, AIAA Paper 2003-2517, July 2003.
- [8] Karpatne, A., and Sirohi, J., "Modeling Internal Flow Through a Rotating Duct Using Quasi 1-D Euler Equations," AIAA Journal, Vol. 54, No. 1, Jan. 2016, pp. 1603–1615.
- [9] Liou, M., and Steffen, C. J., Jr., "A New Flux Splitting Scheme," *Journal of Computational Physics*, Vol. 107, No. 1, 1993, pp. 23–39. 10.1006/jcph.1993.1122
- [10] Churchill, S. W., "Friction-Factor Equation Spans all Fluid-Flow Regimes," *Chemical Engineering*, Vol. 84, No. 24, 1977, pp. 91–92.
- [11] Min, B. Y., and Sankar, L. N., "Hybrid Navier–Stokes/Free-Wake Method for Modeling of Blade-Vortex Interactions," *Journal of Aircraft*, Vol. 47, No. 3, May–June 2010, pp. 975–982. doi:10.2514/1.46550
- [12] Fang, Y., and Menon, S., "A Two-Equation Subgrid Model for Large-Eddy Simulation of High Reynolds Number Flows," 44th AIAA Aerospace Sciences Meeting and Exhibit, AIAA Paper 2006-116, Jan. 2006.
- [13] Spalart, P. R., and Allmaras, S. R., "A One-Equation Turbulence Model for Aerodynamic Flows," *La Recherche Aerospatiale*, AIAA Paper 1992-0439, 1992.
- [14] Dacles-Mariani, J., Zilliac, G. G., Chow, J. S., and Bradshaw, P., "Numerical/Experimental Study of a Wingtip Vortex in the Near Field," AIAA Journal, Vol. 33, No. 9, Sept. 1995, pp. 1561–1568. doi:10.2514/3.12826
- [15] Min, B. Y., and Sankar, L. N., "Enhancements to a Hybrid Navier– Stokes/Free Wake Method for Improved Prediction of Blade-Vortex-Interaction Phenomena," 27th AIAA Applied Aerodynamics Conference, AIAA Paper 2009-3860, June 2009.
- [16] "GridPro v4.1: User's Guide and Reference Manual for TIL, Ggrid and Other Utilities," Program Development Corp., White Plains, NY, Aug. 1999.
- [17] Langston, L. S., "Secondary Flows in Axial Turbines—A Review," Annals of the New York Academy of Sciences, Vol. 934, No. 1, May 2001, pp. 11–26. doi:10.1111/(ISSN)1749-6632